Spectrum of Engineering Sciences
ISSN (e) 3007-3138 (p) 3007-312X Volume 3, Issue 8, 2025

# LOAD FREQUENCY CONTROL USING A NOVEL HYBRID OPTIMIZATION TECHNIQUE FOR SFOPID CONTROLLERS

**Kashif Ali Soomro[1], Imran Ali Bhand[2], Ali Hassan[3], Akhtar Un Nisa[4] , Moula Bux Kanhio[5]**

[1,3]*Department of Electrical Engineering Quaid-e- Awam University of Engineering- Science and Technology Nawabshah, Pakistan.*

[2,4]*Department of Mechatronic Engineering, Mehran University of Engineering and Technology Jamshoro, Pakistan.*

[5]*Institute of mathematics and computer, science, University of Sindh, Jamshoro, Pakistan-*

*Emails: [1]alik85009@gmail.com, [2]ali.imran@admin.muet.edu.pk, [3]a.hasan11mpe16@gmail.com, [4]155.15bme@gmail.com, [5]mbkanhio@gmail.com*

**Keywords** (Dual-area power system; RE control; AOA-RSO; Cascaded fractional-order controller; LFC)

**Article History**
Received on 15 July 2025
Accepted on 25 July 2025
Published on 26 August 2025



**Corresponding Author: ***
**Kashif Ali Soomro**

**Abstract**

Frequency stability in modern power systems is increasingly challenged by the integration of variable renewable energy sources. This study presents a hybrid optimization strategy, combining the Arithmetic Optimization Algorithm and Rat Swarm Optimizer (AOA-RSO), to tune a novel Sigmoid-based Fractional-Order PID (SFOPID) controller for load frequency control. Evaluated on a two-area system, comprising thermal, hybrid PV-wind, and battery storage resources, the proposed controller demonstrates exceptional efficacy. It significantly improves dynamic response, yielding settling times of 20.1 ms and 28.9 ms, a 1.62% reduction in tie-line power deviation, and a minimized ITAE index of 0.2690. Comparative analysis against 20 strategies, including WOA, SMA, and ANN-PID, confirms its superior performance and resilience, underscoring its value for ensuring grid stability with high renewable penetration.

## INTRODUCTION

Maintaining frequency stability has become more and more important for guaranteeing the dependability and effectiveness of interconnected energy networks as RESs have rapidly developed in contemporary power systems. In order to preserve system stability, the integration of these RESs into multi-area power networks creates intricate dynamic interactions that need to be properly controlled [1-5]. Wind energy, Solar can be used to various benefits but still it has stability problems due to variations in load [6-7] This study examines a dual-area power system in which conventional thermal generation is used in one area and solar PV and wind energy are integrated into the other. Furthermore, a BESS is integrated into both regions to increase overall system performance and frequency management. Given the fluctuating load needs and the sporadic nature of solar energy, it is imperative that power generation and consumption be balanced in such systems.

Maintaining this equilibrium while reducing frequency variations and tie-line power transfers between the regions is a significant problem in these systems [8]. In order to keep system frequency within predetermined bounds and guarantee the planned power exchange between areas via the tie-line, LFC is crucial in multi-area power systems [9, 10]. In systems that integrate RESs and have fluctuating power generation, the significance of LFC is increased [11]. Effective LFC tactics are also required to lessen the effect of these oscillations on system stability, which has prompted a great deal of research into sophisticated management and optimization procedures to

improve LFC performance in systems that integrate renewable energy [12]. In order to regulate LFC in two-area systems, several control mechanisms have been investigated. Therefore, proportional-integral (PI), proportional-integral derivative (PID), and their fractional-order counterparts are examples of conventional controllers that have been frequently used [13-16]. Although PI controllers are renowned for being straightforward and simple to use, they could not have the resilience needed for intricate, multi-area power systems. Better response times and stability are provided by PID controllers, which have a derivative component. However, the efficiency of traditional PI and PID controllers might be less than ideal in systems with substantial nonlinearity and temporal delays [5, 14]. A situation like this emphasizes the need for more sophisticated and adaptable control schemes that can manage the dynamic and unpredictable character of multi-area power systems with RESs included.

SFOPID controllers have also been introduced to overcome these issues. In LFC applications, the SFOPID controller in particular provides increased robustness and flexibility. SFOPID controllers offer an extra degree of freedom by integrating fractional calculus into the control strategy, which enables more accurate tuning of the dynamic response of the system. Because of this, they are especially well-suited for two-area systems that incorporate RESs, where the inherent variability and uncertainty necessitate a more complex control strategy[17]. This work uses a novel controller by using an SFOPID controller in light of these factors. The suggested SFOPID controller improves robustness against noise, helps predict future errors, removes steady-state error, and offers more flexibility in adjusting the system's dynamic response.

Optimizing the settings of any control technique, including the SFOPID controller, is crucial to its efficacy. Finding these ideal controller values necessitates sophisticated optimization approaches due to the complexity of LFC in contemporary power systems [18]. The problem's nonlinear and multimodal nature may make traditional approaches ineffective, which is why metaheuristic algorithms are being investigated [19]. In order to increase the controllers' capacity to adjust to changing system conditions, a number of optimization methods have been employed to improve controller parameters as part of the previously described challenge. For instance, LFC in PV-integrated systems has been optimized using the whale optimization algorithm (WOA), which has demonstrated improved performance over conventional techniques [20, 21]. Similarly, the slime mold algorithm (SMA) [22, 23] and the reptile search algorithm (RSA) [24] have been used to enhance control parameters in intricate power systems, showing promise for greatly enhancing control performance in RE settings. Other noteworthy instances include the application of the firefly algorithm (FA) [25] modified grey wolf optimization (MGWO) [26], hybrid shuffled frog-leaping and pattern search algorithm (hSFLA-PS) [27], black widow optimization (BWO) [28], RIME algorithm [29], artificial rabbit optimization (ARO) [30], sea horse optimizer (SHO) [31], and reinforcement learning-based approaches [30] to enhance LFC in similar contexts.

This paper presents the hybrid AOA-RSO as a unique optimization technique to support continued developments in this area. It successfully strikes a balance between exploitation and exploration, which makes it a solid contender to tackle challenging optimization issues like adjusting controller parameters. The AOA-RSO performs exceptionally well in managing the intricacies of LFC in systems that are integrated with RESs, in contrast to earlier optimizers that have had difficulty achieving comparable performance. Using the ITAE as the objective function, the AOA-RSO has been used in this study to adjust the SFOPID controller's parameters in order to guarantee quicker and more

reliable system responses [32], resulting in improved system performance [33]. By efficiently adjusting the SFOPID controller's parameters, the AOA-RSO improves the stability and resilience of dual-area systems that are integrated with BESS and RESs. This method overcomes the drawbacks of traditional controllers and offers an adaptable answer to the changing problems related to the integration of RE [34]. Significant gains in the resilience and durability of RESs and BESS-integrated two-area systems are shown by the performance study of the SFOPID controller, which was optimized using AOA-RSO. The suggested control method increases frequency management by leveraging the benefits of the AOA-RSO and reacts to RESs' dynamic and unpredictable character more successfully [35]. The following is a summary of the contributions:

- The proposed method combines fractional-order control with a modern metaheuristic algorithm, offering a novel solution for the challenges of integrating renewable energy into power grids.
- A key innovation is the use of the AOA-RSO algorithm to optimize an SFOPID controller in a two-area system featuring renewable sources and battery storage.
- This research demonstrates the SFOPID controller's high effectiveness in managing the complex dynamics of systems with significant renewable energy penetration. In order to improve frequency stability, the droop control approach and the BESS's SOC management in [36] is applied, which is coordinated with generator operation, effectively handling large disturbances in uncertain electrical power systems.
- This study demonstrates the AOA-RSO's potential to address intricate power system problems and is among the first to use it in the LFC area.

## 2. Proposed Algorithm

### 2.1 Arithmetic Optimization Algorithm (AOA)

As a novel meta-heuristic optimization technique, the AOA [51] draws inspiration from arithmetic operators' behavior in PC processors or mathematics. Division (D), addition (A), multiplication (M), and subtraction (S) are the four main operations it uses in its computations. The following equation is the math accelerated optimizer (MOA) function that serves as the foundation for the AOA exploitation and exploration phases:

$$MOA(iter) = Min + iter\left(\frac{Max - Min}{Max_{iter}}\right) \quad (1)$$

The variables *iter* and $Max_{iter}$ represent the current and maximum number of iterations, respectively, while *Min* and *Max* denote the accelerated functions corresponding to the minimum and maximum values.

- **Exploration phase:** In the discovery phase, two primary strategies division (D) and multiplication (M) are employed with the objective of identifying the optimal solution. During the exploration stage, positions are updated based on the following equation:

$$x_{i,j}(iter+1) = \begin{cases} best(x_j) \div (MOP + \varepsilon) \times ((ub_j - lb_j) x \mu + lb_j), r2 > 0.5 \\ best(x_j) \div (MOP + \varepsilon) x ((ub_j - lb_j) x \mu + lb_j), otherwise \end{cases} \quad (2)$$

Using $\boldsymbol{x_{i,j}(iter+1)}$, the $i_{th}$ solution's $j_{th}$ position is defined at the current position. $\boldsymbol{best(x_j)}$ represent the best solution realized up till this point at the $j_{th}$ position. The probability math optimizer represents *MOP*, while the control parameter is $\mu$. The following equation shows *MOP*:

$$MOP(iter) = 1 - \left(\frac{iter^{\frac{1}{\alpha}}}{Max_{iter}^{\frac{1}{\alpha}}}\right) \quad (3)$$

∝ represents the sensitive parameter.

- **Exploitation phase:** In this phase of AOA, the addition (A) and subtraction (S) key operators are crucial. The AOA flowchart used during this stage is shown in Figure 1. This phase's goal is to produce dense and highly optimal solutions.

$$x_{i,j}(iter+1)=\begin{cases} best(x_j)-(MOP+\varepsilon)\times((ub_j-lb_j)x\mu+lb_j), r3>0.5 \\ best(x_j)+(MOP+\varepsilon)\times((ub_j-lb_j)x\mu+lb_j), otherwise \end{cases} \quad (4)$$

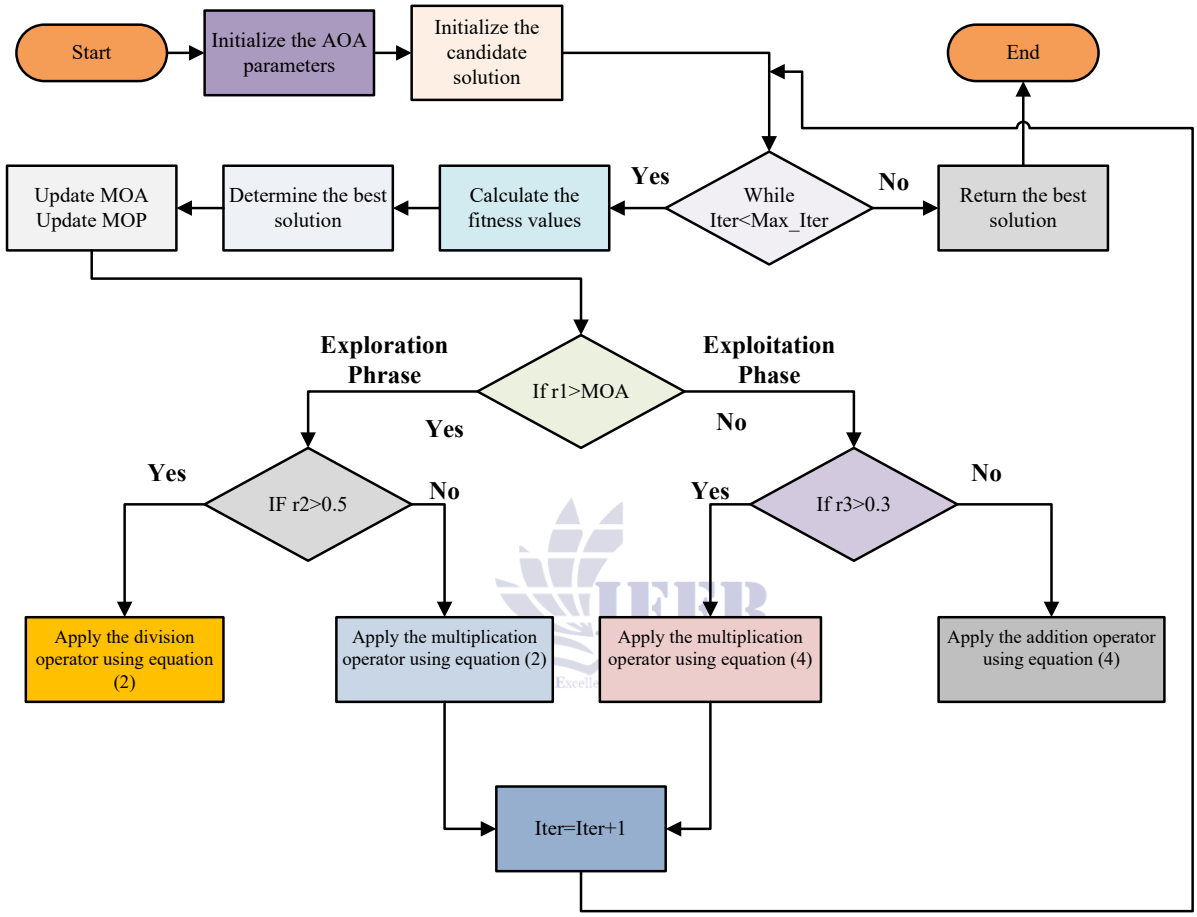


**Figure 1.** AOA Flowchart

*2.2. Rat Swarm Optimization (RSO)*

- This algorithm is inspired by the social behavior of rats. Rats can be classified as animal groupings that include both males and females. Furthermore, this algorithm is primarily motivated by the aggressive nature of rats' behavior. The rat's mathematical model is determined by two essential processes: Fighting and pursuing the prey [52].
- Prey Chasing Phase: During this stage, rats can be thought of as social animals who use specific social agonistic behavior to pursue their prey in groups. Depending on the best search agent for locating the prey's location, a mathematical formulation of the prey chasing process can be provided. According to the most efficient search agent yet achieved, search agents continue to concentrate on their position update. The chasing phase is explained in the following equation:

$$P=A.P_i(x)+C.(P_r(x)-P_i(x)) \quad (5)$$

$$A = R - x \times (\frac{R}{Max_{iteration}}) \quad (6)$$

Where $x$= 0,1,2.... $Max_{iteration}$ and C=2.rand

The parameter C is randomly found in the 1-to-6 range, and R indicates the 0-to-2 random value. Notably, C and A parameters might be used for phases or procedures of exploration and exploitation.

Phase of Fighting with the Prey: This phase examines the fighting process with the prey. A mathematical model that is based on the following equation can be used to depict this process:

$$P_i(x+1) = |p_r(x) - P| \quad (7)$$

Based on the subsequent position, the updated rat position is shown by $P_i(x+1)$. Furthermore, the best position is saved because it is the most optimal solution to date, and its update depends on the best search agent. It is observed that the rat in (A, B) may be able to update its position while traveling toward the prey $A^*, B^*$. The updated parameters for many or different positions that are attained by the position now attained are represented by equations 5 and 7. Therefore, C and A parameters are used to modify the exploration and exploitation stages. Figure 2 depicts the RSO flowchart.

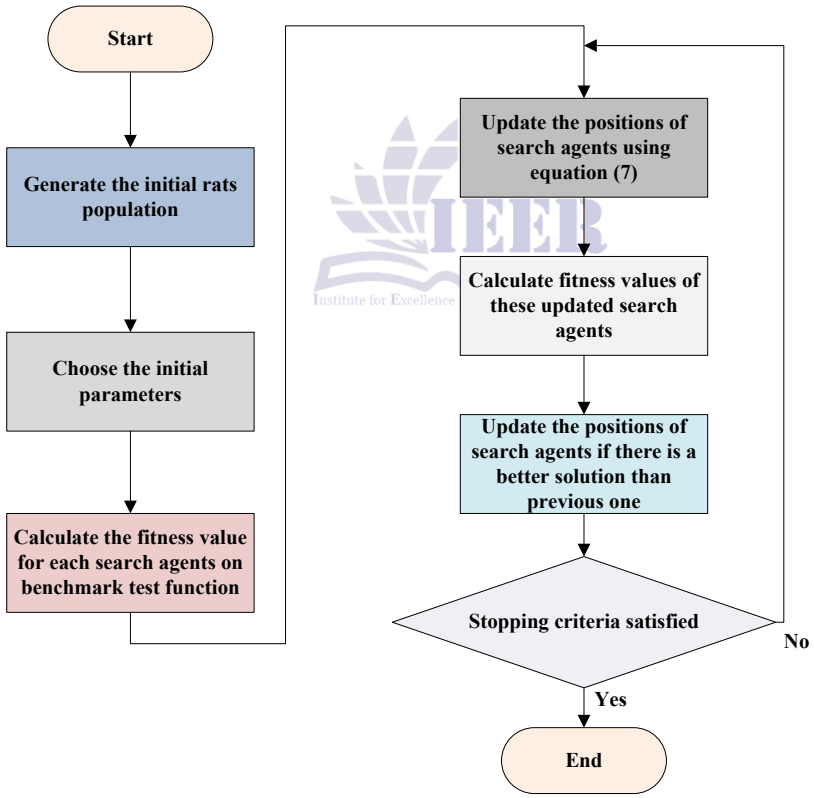


**Figure 2.** RSO flowchart

*2.3. Hybrid AOA-RSO Algorithm (HAOARSO)*

In the AOA algorithm, each individual undergoes either the exploitation phase utilizing the Addition or Subtraction operator or the exploration phase employing the Multiplication or Division operator. Simultaneously, in the RSO algorithm, every individual performs two key actions: pursuing the prey and battling with it. The Hybrid AOA-RSO Algorithm runs separate phases of the RSO and

AOA algorithms in simultaneously. Both the RSO and AOA algorithms operate on the same population. After combining the populations produced by the two algorithms, the best half of the population is chosen to serve as the starting population for the following iteration. Algorithm 1 presents the pseudocode of the HAOARSO algorithm, while its flowchart is illustrated in Figure 3.

Complexity, computing time, and the choice of input parameters such as constant Parameter $\mu$, *MOP-min*, Y, *MOP-max*, and Alpha control parameter (X) for the hybrid algorithm are some of the disadvantages and restrictions of the suggested approach. The suggested HAOAROA algorithm goes through 95 runs and takes longer to choose the best settings for better performance in order to address these problems.

**Stage 1 (Initialization):**

**Step1:** Initial Set the maximum number of iterations (MaxIt), population (nPop), AOA parameters (MOP_Max, MOP_Min, Alpha, and Mu), and RSO parameters (R)

**Step2:** Set the random population K to its initial values

**Step3:** Determine the original population's fitness values

**Step4:** From the starting population set iter=1, find the optimal solution Kbest

**Step5:**

- Set the AOA and RSO populations both as K, i.e., $K_{aoa} = K_{rso} = K$
- Set the AOA and RSO fitness values both as f i.e., $f_{aoa} = f_{rso} = f$
- Update the value of MOP using Equation:

$$MOP(iter) = 1 - \left(\frac{iter^{\frac{1}{\alpha}}}{Max_{iter}^{\frac{1}{\alpha}}}\right) \quad (8)$$

- Use Equation to update the MOA value:

$$MOA = MOP\_Min + It \times \left(\frac{MOP\_Max - MOP\_Min}{MaxIt}\right) \quad (9)$$

- Use the following equation to update the value of A:

$$A = R - R \times \left(\frac{It}{MaxIt}\right) \quad (10)$$

**Stage 2 (AOA Phase):**

**Step6 (AOA Phase):**

- Generate a random number $r_1$
- If r1> MOA then, Exploration phase

  Generate random number $r_2$

- If $r_2$> 0.5

  Apply Division Math operator (÷)

  Calculate the positions of solutions (gorillas) using:

$$K\_new_{i,j} = \frac{K_{silverbackj}}{(MOP + eps)} \times ((K_{\max j} - K_{\min j}) \times Mu + K_{\min j}) \quad (11)$$

- Else, Apply Multiply Math operator (*)

  Calculate positions of solutions (gorillas) using Eq:

$$K_{new_{i,j}} = K_{silverbackj} \times MOP \times ((K_{\max j} - K_{\min j}) \times Mu + K_{\min j}) \quad (12)$$

- Else, Exploitation phase
- If r > 0.5

  Apply Subtraction Math operator (-)

  Calculate positions of solutions (gorillas) using:

$$K_{new_{i,j}} = K_{silverbackj} - MOP \times ((K_{\max j} - K_{\min j}) \times Mu + K_{\min j}) \quad (13)$$

  Apply Addition Math operator (+)

  Calculate the positions of solutions (gorillas) using:

$$K_{new_{i,j}} = K_{silverbackj} + MOP \times ((K_{\max j} - K_{\min j}) \times Mu + K_{\min j}) \quad (14)$$

  Where, $i$ is the population member and $j$ are the dimension.

  Calculate the fitness values of Gorilla

- If New Solutions ($K\_new$) are better than previous solutions ($K_{aoa}$), replace them.
- Update $K_{best}$ as the location of silverback (best location)

**Step 7 (RSO Phase):**

- Search agents update their positions with respect to best search agent obtained so far using:

$$P\_vec = A \times K_{rsoi,j} + abs(C \times K_{bestj} - K_{rsoi,j})) \quad (15)$$

  Where $i$ is the population member and $j$ are the dimension.

- Fighting process of rats with prey, update the position of Search Agents using equation:

$$K_{rsoi,j} = K_{bestj} - Pvec)) \quad (16)$$

- Calculate the fitness values of Search Agents (individuals)
- Combine population of both AOA ($K_{aoa}$) and RSO ($K_{rso}$) and take the best half of the population
- Update the best position $K_{best}$ and fitness value $f_{best}$.

  Iter = Iter + 1

- While (Iter < MaxIt)

  Return best solution i.e, $K_{best}$, and $f_{best}$

## 3. Modeling of the Proposed Power Architecture

Following section describes the mathematical formulation of the proposed power configuration [15].

### 3.1. Thermal Power Elements

Key elements of thermal power consist of governor, turbine, and load. Each of these components is essential for system's functioning and stability.

**Governor:** Governor is a mechanical device used to monitor and regulate an engine's speed. Its main purpose is to regulate the engine's average speed when load fluctuates. The block diagram of velocity governor for a power network is illustrated in Figure 3. In this figure, governor's time $T_G$ , and speed governing mechanism is revealed with an unstable fall correction $G_c(s)$. Other parameters include mechanical generator opening time $T_M$, duty ratio $D$, droop gain $R$, turbine time $T_r$, vary in frequency $\Delta f$, alteration in generator power output $\Delta P$, turbine's mechanical power output change $\Delta P_m$ , and power load change $\Delta P_L$.

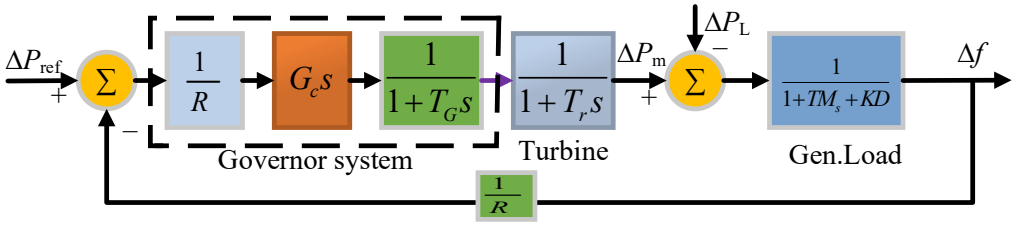


Figure 3. Speed governor illustration.

**Turbine:** Turbine is a rotational device that generates useful work by transforming energy from the movement of a liquid, like steam, water, or air, into rotational motion. Figure 4 represents transfer function model of turbine. The time delay between valve's switching position and torque of turbine is indicated by $T_{ch}$ .

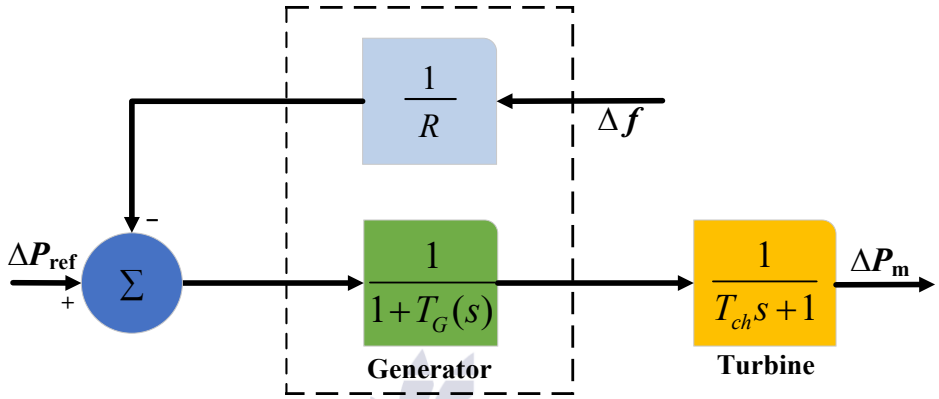


Figure 4. Turbine transfer function illustration.

**Load:** Power grid encounters different load types. Figure 5 depicts load model, while $H$ stands for generator inertia coefficient, and $\Delta P_e$ represents modification in electrical power.

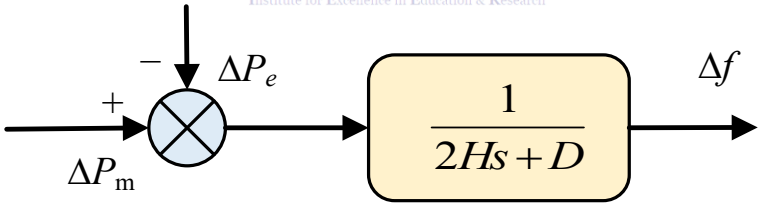


Figure 5. Load model illustration.

$$\text{Governor} = \frac{1}{1+sT_{sg}} \tag{17}$$

$$\text{Reheater} = \frac{1+sK_rT_r}{1+sT_r} \tag{18}$$

$$\text{Steam generator} = \frac{1}{1+sT_t} \tag{19}$$

Time coefficients for steam turbine, reheater, and governor are indicated, $T_{sg}$, $T_r$, & $T_t$. Figure 6 illustrates, demonstration of a one-area thermal power.

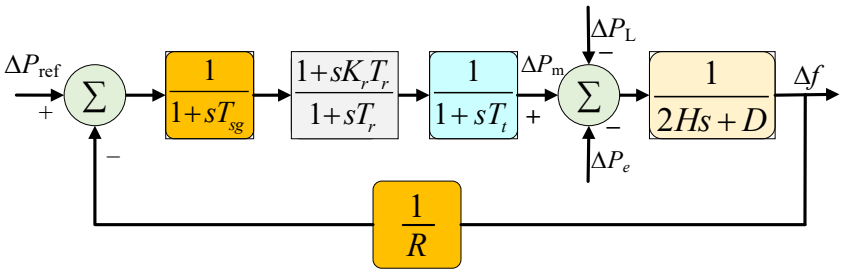


**Figure 6.** Representation of one-area thermal energy network.

Governor, turbine, and load elements are linked together to create thermal power network. Governor regulates the mechanical power output of turbine $\Delta P_m$ in reaction to variations in frequency $\Delta f$ and load $\Delta P_L$. The turbine subsequently transforms this machine-driven energy into electrical energy, which is fed to grid. Load element illustrates the fluctuations in electrical power consumption, affecting overall constancy and efficiency of power system.

### 3.2. Numerical Modeling of Wind Power Network

The following is an explanation of the wind power system demonstration:

**Wind speed modelling:** Wind energy system plays a vital role in determining the electricity generation potential. Under optimal conditions, power that wind turbines can extract is proportional to cube of wind velocity. Kinetic energy given as:

$$E = \frac{1}{2}mv^2 \tag{20}$$

Where $m$ shows moving mass of air and $v$ motion speed. At that time, wind speed reports as:

$$P_{wind} = \frac{E}{\Delta t} \tag{21}$$

Generally, a scalar purpose that evolves to depict wind velocity V, it can also be separated into two distinct elements, which illustrate changes in wind, with one portion that changes gradually, indicated as $V_0$, and a component that changes unpredictably, referred to as $V_t$. Following, wind velocity can be communicated as:

$$V = V_0 + V_t \tag{22}$$

Previous work presents three approaches for mathematically demonstrating wind velocity profile:

Initial method involves a white noise straining system that employs a low-pass filter with a subsequent transferal purpose to mitigate the effects of commotion:

$$F(s) = \frac{1}{1+\tau.s} \tag{23}$$

While τ is time constant that depends on average wind speed, rotor diameter, and level of wind turbulence.

2nd method for generating a wind velocity profile employs established spectral density by meteorologist I. Van der Hoven to describe variations in wind velocity. Consequently, wind velocity fluctuation V represented:

$$V_v = A + \sum_{i=1}^{n} \alpha_k . \sin \times \omega_k . t \tag{24}$$

In wind outline scheming, final harmonic rank is represented by $i$, while $\alpha_k$ denotes largeness of K-order modulation, $\omega_k$ indicates vibration of K-order intonation, and A refers to usual wind speed.

3rd method involves Weibull dissemination, which assesses regular wind velocity over specific time intervals to evaluate wind potential at a particular location. Subsequently, a histogram organizes the collected data into numerical values based on classifications of wind speed. Taking into account the specified time and Weibull probability distribution, wind profile can be represented:

$$V_v = (1 + \xi_v - \xi_v).V_v \tag{25}$$

$\xi_v$ mean value of disturbance and $V_v$ mean wind velocity:

$$\xi_v = \left(-\frac{\ln(rand)}{C_v}\right)^{\frac{1}{k_v}} \tag{26}$$

In context of analyzing wind class histograms, ($C_v$, $k_v$) represents a pair of parameters. Additionally, *rand* is a expression that produces arbitrary values uniformly between 0 and 1.

**Modelling of wind turbine:** Wind power stands as a key nontraditional foundation of energy. It

operates through a wind power system, where the capability of wind turbine generator (WTG) is integrated with current energy grid [37-39]. Vibrant model for WTG is outlined below:

$$\Delta P_{WTG} = \frac{1}{T_{WTG}} \Delta Pw - \frac{1}{T_{WTG}} \Delta P_{WTG} \quad (27)$$

$Pw$ represents wind power, $T_{WTG}$ refers to WTG time continual, and $\Delta P_{WTG}$ indicates change in output power of WTG. Rotor of turbine, outfitted with vanes, converts wind energy into mechanical power. Subsequent equations can be employed to mathematically describe wind power harnessed by rotor[38]:

$$P_{rotor} = \frac{1}{2} \rho A V^3 C_p \quad (28)$$

In this context, $A$ represents swept area, $V$ refers to wind velocity, $C_p$ denotes power constant, and $\rho$ signifies wind compactness. Connection among input wind speed and active power is illustrated as follows:

$$P_{GW} = \frac{\rho a^2 V_\omega^3 C_p}{2} (T_{SR}, \beta) \quad (29)$$

$\beta$ shows pitch angle, $T_{SR}$ tip speed ratio, $\alpha$ area density, $V_\omega$ wind velocity. Rotor efficiency $C_p$:

$$C_p = \frac{T_{SR} - 0.022\beta^2 - 5.6}{2} e^{-0.17 T_{SR}} \quad (30)$$

$$T_{SR} = \frac{r_{pm} \pi D}{60V}$$

Turbine produced torque given as:

$$T_t = \frac{P_{GW}}{\omega t} \quad (31)$$

While $\omega t$ represents angular velocity of wind turbine rotor.

**Gearbox Modelling:** Mechanical components of a wind turbine consist of turbine spindle, turns slowly at a pace of $\Omega_t$, gear assembly that features increase in G, enabling it to drive generator at a faster speed of $\Omega_g$ via a secondary spindle.

Utilizing gear assembly, rotor speed $\Omega_t$ could be enhanced via multiplication gain G to synchronize with generator's high velocity $\Omega_g$. Deformation, resistance, and energy dissipation associated with gear assembly are considered negligible, which enhances efficiency of this device. Succeeding two equations illustrate the calculated model governing operation of this equipment:

$$T_g = \frac{T_{aer}}{G}$$
$$\Omega_t = \frac{\Omega_g}{G} \quad (32)$$

In case of $T_{aer}$ wind turbine, aerodynamic torque is indicated by $\Omega_g$, speed of generator shaft is represented as $\Omega_g$, and $T_g$ refers to torque on generator shaft. Multiplication gain, denoted as G and $\Omega_t$ turbine velocity spindle. Inertia $J$, which can be articulated by following equation:

$$J = \frac{J_t}{G^2} + J_g \quad (33)$$

Constant of friction for generator $f_g$ and constant of friction for turbine $f_t$ constitute total viscous friction constant $f_v$, given as:

$$f_v = \frac{f_t}{G^2} + f_g \quad (34)$$

Net mechanical torque $T_{mec}$, Controls generator's rotational speed $\Omega_g$. This torque represents total of all torques acting on generator shaft $T_g$ (generator torque), $T_v$ (viscous friction torque), and $T_{em}$ (generator's electromagnetic torque).

$$T_{mec} = J \times \frac{d\Omega_g}{dt} \quad (35)$$

$$T_{mec} = T_g - T_{em} - T_v \quad (36)$$

$$T_v = f \times \Omega_g \quad (37)$$

As a result, the following expresses the differential equation governing the dynamics of a mechanical network:

$$J \times \frac{d\Omega_g}{dt} = T_g - T_{em} - T_v \quad (38)$$

This paper concentrates on the output generation of a Wind-powered turbine, particularly utilizing a Permanent Magnet Synchronous Generator (PMSG). Figure 7 depicts schematic diagram of the PMSG wind generator that uses P & O MPPT. Control system for wind generator incorporating PMSG has been created in MATLAB/Simulink. In Figure 7 $V_\omega$, $\beta$, $T$, $\omega$ and $D$ represents the angular velocity, pitch angle, toque generator rotation and duty cycle. The equations below mathematically illustrate the PMSG wind turbine [41, 42].

$$\frac{dw_{gen}}{dt} = \frac{1}{2H_{gen}}\left[-\frac{P_{elec}}{w_{gen}+w_0} - D_{tg}(w_{gen}-w_{rot}) - k_{tg}\Delta\theta_m\right] \quad (39)$$

$$\frac{dw_{rot}}{dt} = \frac{1}{2H_{rot}}\left[-\frac{P_{mech}}{w_{rot}+w_0} + D_{tg}(w_{gen}-w_{rot}) + k_{tg}\Delta\theta_m\right] \quad (40)$$

$$\frac{d(\Delta\theta_m)}{dt} = w_{base}(w_g - w_t) \quad (41)$$

$w_{gen}$ denotes speed of generator, $P_{elec}$ electric power, $w_0$ initial velocity, $w_{rot}$ turbine speed, and $P_{mech}$ mechanized power; stable state appears when $w_{gen}$ = $w_{rot}$, so $d(\Delta\theta)/dt = 0$, & $P_{elec} = P_{mech}$. $D_{tg}$, $K_{tg}$, & $w_{base}$ are constants [43]. Mass's geometrical dissipation demonstrates inertial constant, inertial moment evaluated utilizing:

$$H_{rotor} = \frac{J_{rotor}w_{rotor}^2}{2P_n}; H_{gen} = \frac{J_{gen}w_{gen}^2}{2P_n} \quad (42)$$

Wind rotor's period of inactivity can be eliminated by:

$$J_{rotor} = \frac{1}{8}m_r R^2 \quad (43)$$

Mass and radius of rotor are denoted by symbols $m_r$ and $R$, respectively. Stator terminal Generator output voltages in d-q frame expressed as:

$$V_d = R_d I + L_d \frac{dI_d}{dt} - \omega_{gen} L_q I_q \quad (44)$$

$$V_q = R_q I_q + L_q \frac{dI_q}{dt} + \omega_{gen}(L_d I_d + \varphi_f) \quad (45)$$

$L$ shows inductance of generator's, $R$ resistance, $I$ Current along d-q coordinates, $\varphi_f$ permanent magnetic flux, and $\omega_{gen}$, PMSG's spinning speed.

$$\omega_{gen} = P_p \omega_{ref} \quad (46)$$

$P_p$ represents pole pairs. Electromechanical rotational torque $T_{gen}$, given as:

$$T_{gen} = \frac{3}{2}P_p\omega_{ref}((L_q - L_d)i_d i_q + \varphi_f i_q \quad (47)$$

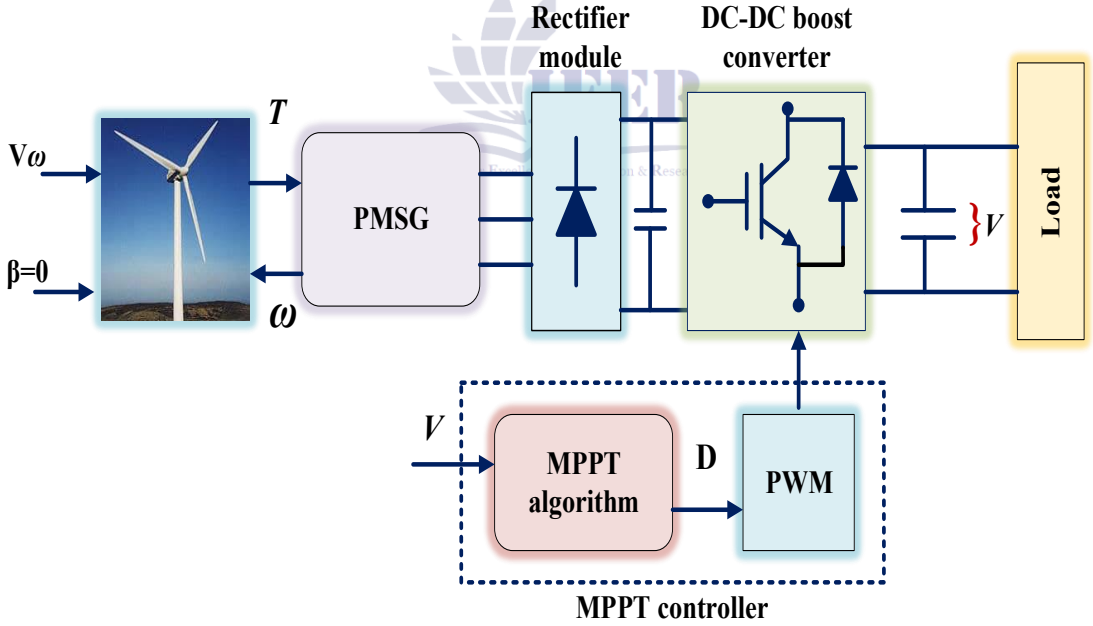


Figure 7. Illustration of PMSG wind network.

### 3.3 PV framework

Similar to WTGs, PV systems are variable power sources that primarily rely on the amount of solar light and surface temperature [44]. These factors are used to calculate the PV system power using Equation (48), which looks like this:

$$P_{PV} = \varphi S \xi\left(1 - 0.005\left(T_A - 25\right)\right) \quad (48)$$

Where, $\varphi$ fall within (9%-12%), S is efficiency of PV array; S is efficiency of PV panels cover ($m^2$);

$\xi$ is solar irradiance (kW/m$^2$); $TA$ often standardized at 25◦C, is ambient temperature.

The PV system in the identical scenario with WTGs is defined by a first-order lag transfer function, which is described in Equation (49) as follows:

$$G_{PV}(s) = \frac{\Delta P_{PVG}}{\Phi PV} = \frac{K_{PV}}{1 + sT_{PV}} \quad (49)$$

This study describes a fuzzy logic-based MPPT PV approach using MATLAB/Simulink. Block diagram of control method, which integrates fuzzy MPPT technique is shown in Figure 8. In Figure 8; $I_{PV}$, $V_{PV}$, $p$, $S$, and $D$ show PV current, voltage, power, switch, and diode.

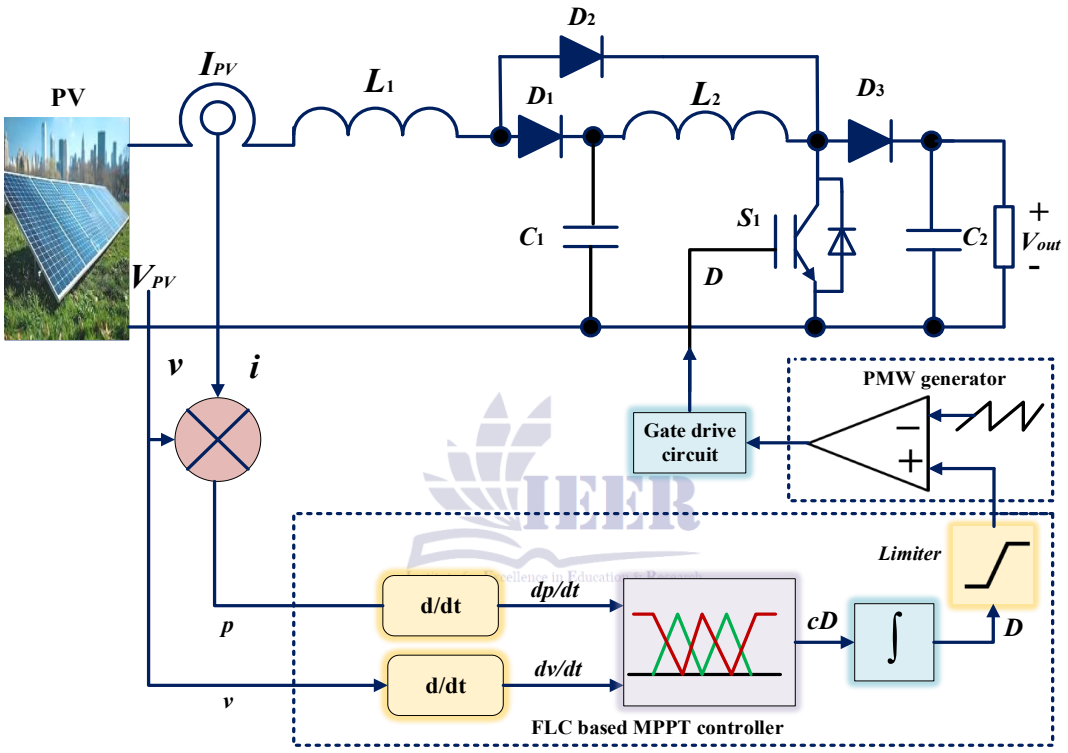


Figure 8. Schematic illustration of fuzzy MPPT solar system.

### 3.4 BESS framework with droop regulation

In addition to the robust growth of RESs, BESS has been assessed as a backup function to balance load demand and power supply in LFC over the last ten years. BESS devices are able to achieve precise frequency management by utilizing droop control to modify the state of charge (SOC) from LFC output [36].

#### 3.4.1 SOC estimation of BESS

Frequently, system current is used to calculate the battery's state of charge. If the battery's interval voltage is contracted, the system is proportionate to the current. Lastly, by applying the energy idea by the transfer function and integrating power as Equations (50) and (51), we can directly ascertain the SOC of BESS:

$$SOC(t) = SOC_0 + \frac{1}{Eh}\int_{t_0}^{t} P_{BESS}(t)\,dt \quad (50)$$

$$\frac{\Delta SOC(s)}{\Delta P_{BESS}} = \frac{1}{Eh} \times \frac{1}{s} = \frac{1}{K_E s} \quad (51)$$

where $SOC_0$ is the initial value of SOC; $E$ is a battery capacity (MWh); $h$ is a factor of hour second (h=3600); PBESS is a battery power (MW); $\Delta SOC = SOC - SOC_0$ and $K_E$ is BESS energy in

joule (BESS capacity in accordance the number of seconds).

As shown in the following equation, the droop rate is determined when frequency fluctuations result in electricity being supplied to the grid:

$$\Delta P_{BESS}(t) = \frac{1}{R_{BESS}} \Delta f(t) \quad (52)$$

The relationship between SOC and frequency is displayed here, based on the relationship between SOC and power in Equation (51) and droop in Equation (52):

$$\frac{\Delta SOC(s)}{\Delta f(s)} = \frac{1}{R_{BESS}} \times \frac{1}{Eh} \times \frac{1}{s} = \frac{1}{R_{BESS} K_E s} \quad (53)$$

### 3.4.2 Droop control with SOC feedback-based offset

The droop control with SOC feedback is introduced in [36] with the main purpose of managing power flow, which complements LFC.

Based on Equation (53), to determine the BESS power in Equation (54), we subtract the frequency offset from the initial frequency variation.

$$\Delta P_{BESS}(t) = 1\frac{1}{R_{BESS}} \left[\Delta f(t) - f_{o f_s}(t)\right] \quad (54)$$

$$f_{ofs}(t) = \Delta SOC(t) K_f \quad (55)$$

$$K_f = \frac{f_{ofs},max - f_{ofs},min}{SOC_{tot}} \quad (56)$$

In a large-scale system, installing multiple BESSs simultaneously is crucial, it brings sustainability and stability to the EPS based on reducing dramatic peak frequency fluctuations in the shortest possible time.

For BESS aggregation, installing BESS parallel with droop control can be represented as $R_{BESS}/Y$, where $Y$ indicates the number of parallels. The capacity of the BESS can be expressed as $XKE$, where $X$ signifies multiple BESS units. Figure 9 depicts the detailed block diagram of BESS with droop control applied for LFC in EPS

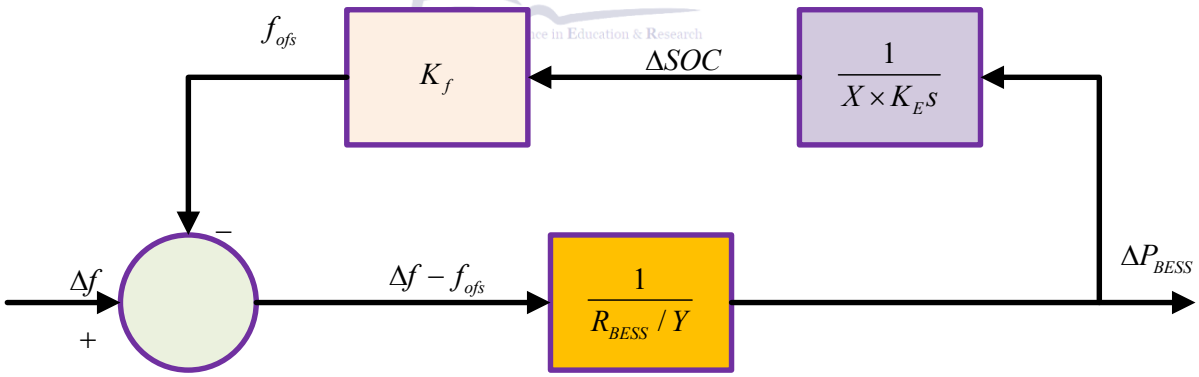


Figure 9: SOC feedback-based droop control with offset [34].

The tie-line, which promotes power exchange, controls the relationship between the two sectors. The power flow in the tie-line is represented by

$$\Delta P_{tie}(t) = \frac{2\pi T_{12}}{s}\left(\Delta f_1(t) - \Delta f_2(t)\right) \quad (57)$$

The frequency deviations in the respective areas are represented by $\Delta f_1(t)$ and $\Delta f_2(t)$, while $T_{12}$ denotes the synchronizing coefficient. A detailed model is presented for analyzing and optimizing the dynamics and control strategies of the proposed power system, with the parameters outlined in Tables 1 and 2.

Table 1. Constraints values of thermal power network.

| Restraint | Restraint value |
|---|---|
| Turbine constant time | 0.5 s |

| | |
|---|---|
| Governor time constant | 0.2 s |
| Generator moment of inertia | 5 s |
| Governor's speed control | 0.05 Pu |
| Turbine power capacity | 250 MW |
| Frequency | 60 Hz |
| Duty cycle | 0.8 |

Table 2. Constraint values and electrical configurations of wind, solar, and BESS systems.

| | |
|---|---|
| Features of PV | |
| Parallel strings | 90 |
| Module connected in series | 55 |
| Maximal output power | 213.15 W |
| Voltage in an open circuit | 36.3 V |
| Voltage at peak power | 29 V |
| Temperature coefficient of open-circuit voltage | −0.36099 |
| Every module's cell | 60 |
| Short circuit current | 7.84 A |
| Current at peak power | 7.35 A |
| Thermal coefficient | 0.102 |
| Specified temperature | 25 °C, 1000 (W/m$^2$) |
| Ideal diode factor | 0.98117 |
| Resistance in parallel | 313.3991 ohm |
| Series resistance | 0.39383 ohm |
| **Characteristics of PMSG wind turbine** | |
| Mechanical output power | 1400 kW |
| Base power of generator | 1400 kW/0.94 |
| Peak power (Pu) | 0.95 |
| Rotational speed of generator (Pu) | 1.1 |
| Stator phase resistance | 0.0578 ohms |
| Wind speed | 12 m/s |
| BESS | |
| $K_f$ | 0.1/60 |
| $K_E$ | 1.8 |
| $R_{BESS}$ | 0.2 |

## 4. An Innovative Approach to LFC

### 4.1 Real PID Model

The actual PID controller is depicted in Figure 10 and primarily consists of (58) of four parameters that need to be adjusted: Filtering coefficient N, integral gain $K_i$, derivative gain $K_d$, and proportional ga. in $K_p$ [15].

$$C(s) = K_p + \frac{K_i}{s} + \frac{NK_d}{1+N/s} \tag{58}$$

The Real PID controller constraints are as follows:

$0 \le k._p \le 10$, $0 \le k._i \le 10$, $0 \le k._d \le 10$, $0 \le N \le 95$

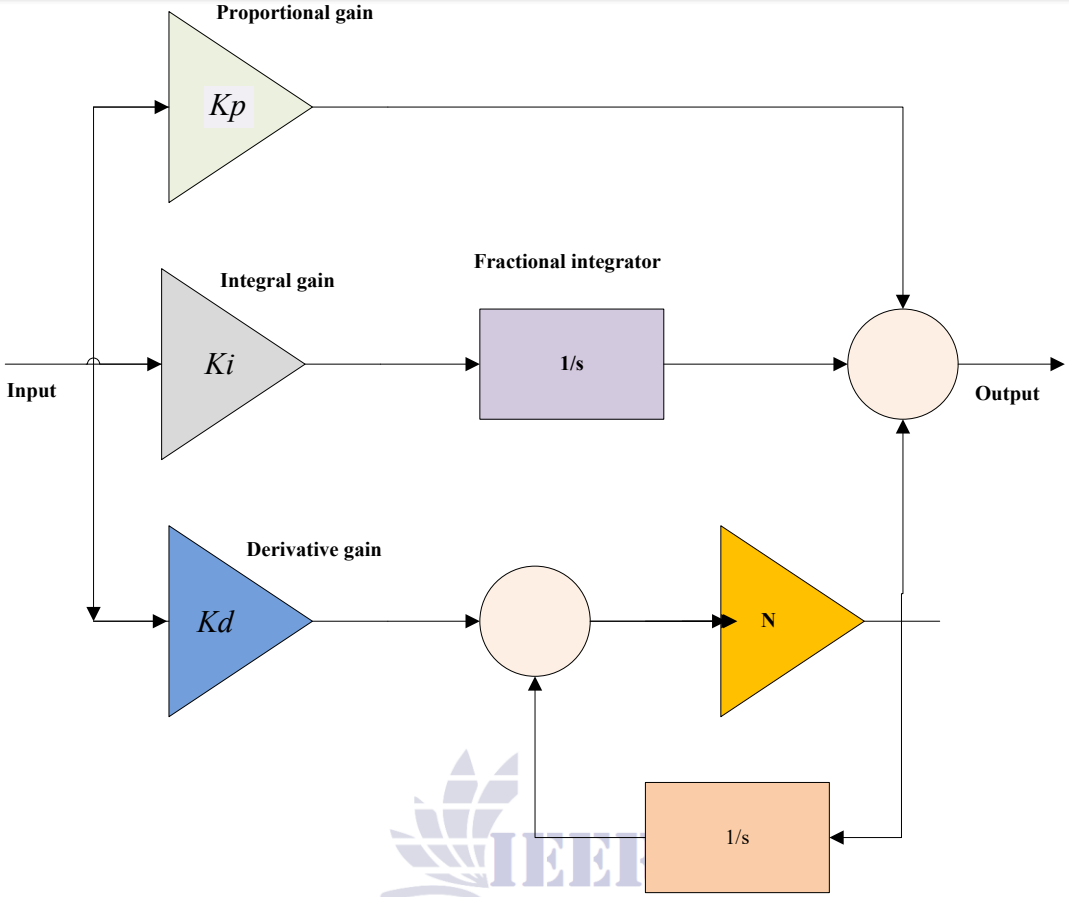


Figure 10 Block diagram of real PID controller.

### 4.2 FOPID Model

Equation (59) shows that the fraction Order PID (FOPID) controller in Figure 11 is primarily composed of five gains: The fractional integrative coefficient $\lambda$, the fraction derivative coefficient $\mu$, the derivative gain $K_d$, the proportional gain $K_p$, and the integrative gain $K_i$ come first, second, and third, respectively [45-47].

$$C(s) = K_p + \frac{K_i}{s^{\lambda}} + K_d s^{\mu} \tag{59}$$

The following are the FOPID controller constraints:

$0. \leq k._p, \leq 10,\ 0. \leq k._i \leq 10,\ 0 \leq k_d \leq 1.0,\ 0 \leq \lambda \leq 1,\ 0 \leq \mu \leq 1$

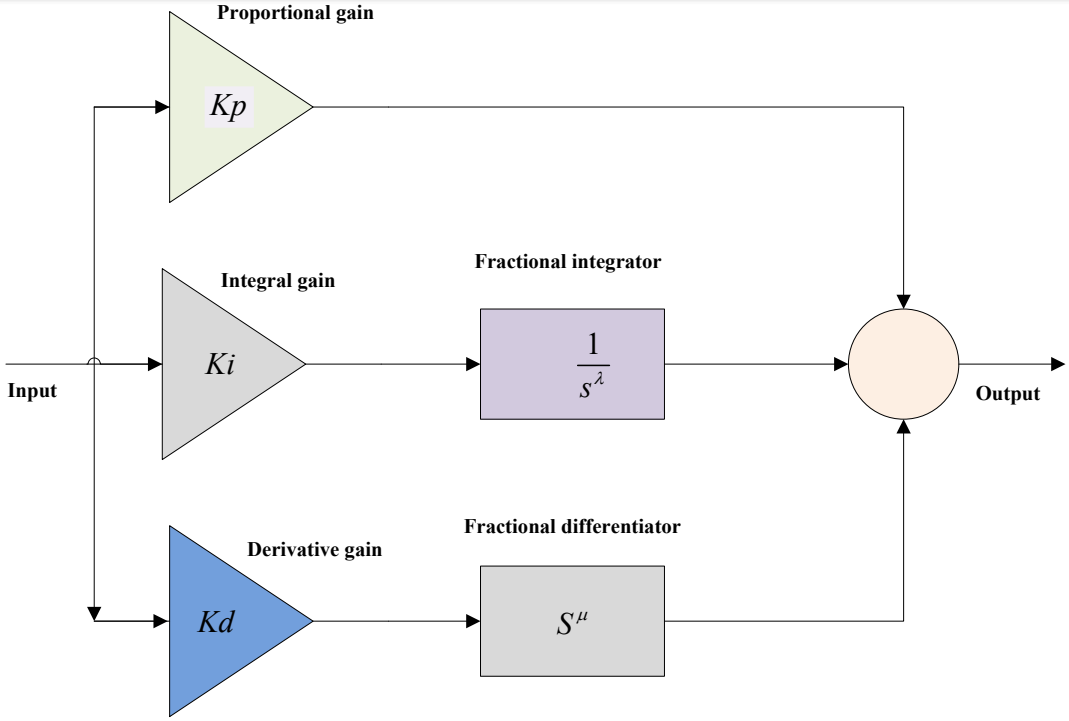


Figure 11 Block diagram of Fractional Order PID controller.

### 4.3 SFOPID Model

A sigmoid fractional order PID (SFOPID) controller is depicted in Figure 12. This controller's goal is to create a more appropriate control response by substituting proportionately updated parameters based on the error dynamics for the preset controlling parameters in the conventional control response. It should be mentioned that in a conventional PID controller, the experiment simulation maintains all of the parameters at the same level. Keeping these control parameters, constant weakens the overall control's precision and resilience. The sigmoid PID controller parameters in (60–63) have upper bounds of $k_{phi}$, $k_{ihi}$, and $k_{dhi}$, and lower and higher bounds of $k_{plo}$, $k_{ilo}$, and $k_{dlo}$. Additionally, to overcome and adjust the sharpness of the transition between upper and lower bounds, the parameters $\sigma_p$, $\sigma_i$, and $\sigma_d$ are constants. The fractional order parameters are $\lambda$ and $\mu$. For the derivative portion, $N$ is a filtration coefficient that has a constant value of 95. The SFOPID controller's mathematical formulas are:

$$k_{pv}(t) = k_{plo} - \left| \frac{k_{phi} - k_{plo}}{1 + e^{-\sigma p |e(t)|}} \right| \tag{60}$$

$$k_{iv}(t) = k_{ilo} - \left| \frac{k_{ihi} - k_{ilo}}{1 + e^{-\sigma i |e(t)|}} \right| \tag{61}$$

$$k_{dv}(t) = k_{dlo} - \left| \frac{k_{dhi} - k_{dlo}}{1 + e^{-\sigma d |e(t)|}} \right| \tag{62}$$

$$C(s) = k_{pv}(t) + \frac{k_{iv}(t)}{s^{\lambda}} + \frac{N k_{dv}}{1 + N / S^{\mu}} \tag{63}$$

It should be mentioned that the $k_{pv}$ (t), $k_{iv}$ (t), and $k_{dv}$ (t) in (60-62) are not held constant, but rather alternate to the error signal. To keep designing parameter tuning as simple as possible we define $\Delta p = |k_{phi} - k_{plo}|$, $\Delta i = |k_{ihi} - k_{ilo}|$ and $\Delta d = |k_{dhi} - k_{dlo}|$. N is the filter constant with a value of 95. The SPID controller constraints are as follows:

$0 \le k_{plo} \le 20$, $0 \le \Delta p \le 0.1$, $0 \le \sigma p \le 20$, $0 \le k_{ilo} \le 20$, $0 \le \Delta i \le 0.1$, $0 \le \sigma i \le 20$, $0 \le k_{dlo} \le 20$, $0 \le \Delta d \le 0.1$, $0 \le \sigma d \le 20$, $0 \le \lambda \le 1$, $0 \le \mu \le 1$

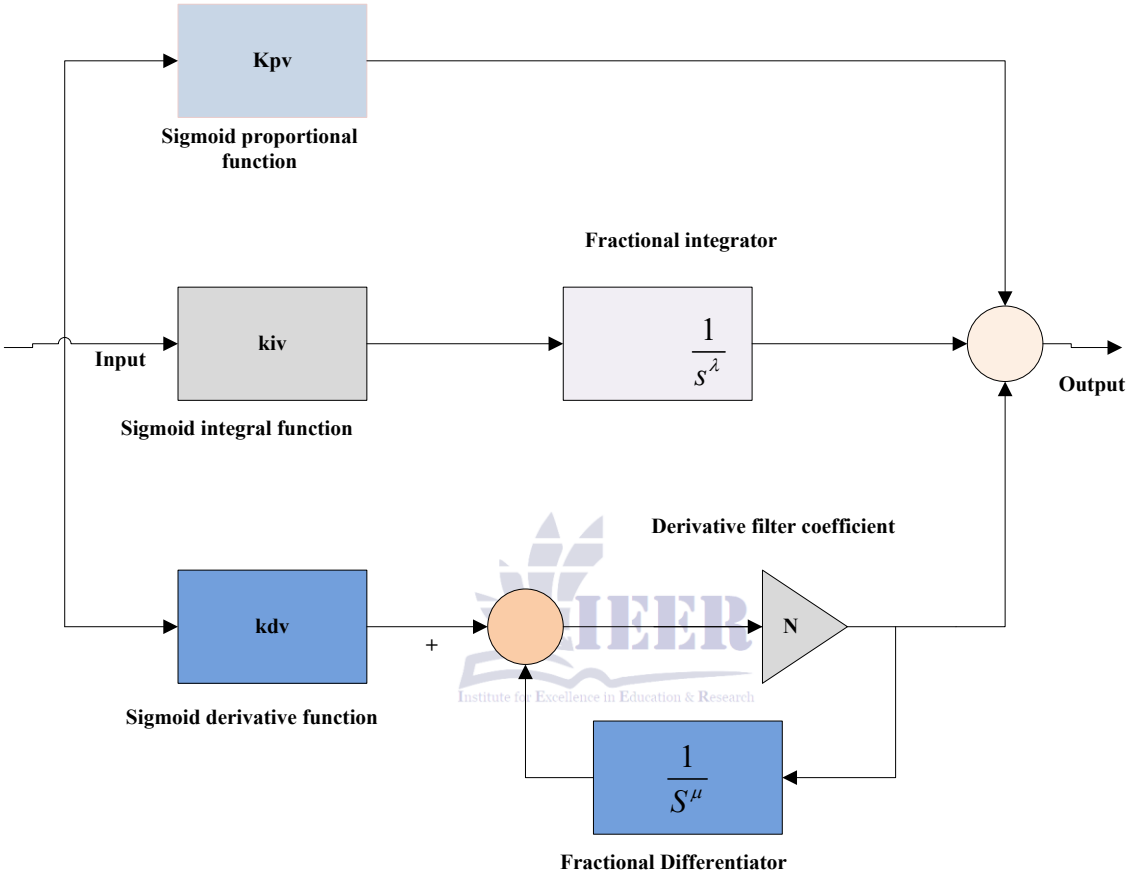


Figure 12 Block diagram of Sigmoid PID controller.

In order to promote faster and more consistent system responses, this control technique seeks to reduce the Integral of ITAE, a performance measure that prioritizes lowering mistakes over time [31]. Equation (64) provides a mathematical representation of the objective function.

$$F_{ITAE} = \int_0^{T_{sim}} \left( |\Delta f_1| + |\Delta f_2| + |\Delta P_{tie}| \right) \times t \times dt \qquad (64)$$

where the whole simulation duration is denoted by $T_{sim}$ = 50 s. The frequency variations in Area 1 and Area 2 are denoted by $\Delta f_1$ and $\Delta f_2$, respectively. The difference in tie-line power between the two regions is denoted by $\Delta P_{tie}$. Finding a controller setup that reduces these aberrations and speeds up system stability restoration is the aim. This model's validity encompasses normal operating conditions, such as load fluctuations and disruptions, in multi-area power systems.

## 5. Results and Discussion of the Simulation

### 5.1. Statistical Success of the AOA-RSO

The AOA-RSO is statistically compared with other popular metaheuristic algorithms WOA, SMA, RSA, and ARO based on their ability to

minimize ITAE in a two-area power system over 30 runs. Parameter settings for each algorithm, including population size and control variables, are detailed in Tables 3 and 4. Notably, the number of function evaluations (NFE) significantly impacts algorithm efficiency, with 4600 identified as the optimal value for balancing accuracy and computational cost across all algorithms tested[3, 20, 25-27, 29, 32, 33, 48].

Table 3. Values of the proposed algorithms' parameters.

| Technique | Population size | Evaluation function | Parameters |
|---|---|---|---|
| WOA [19] | 80 | 4600 | a = [0, 2], a2 = [−3, −1] and b = 1 |
| SMA [20] | 80 | 4600 | z =0.05 |
| RSA [22] | 85 | 4600 | $\alpha$ =0.2 and $\beta$ = 0.3 |
| ARO [28] | 90 | 4600 | - |

Table 4. Parameters of Hybrid AOA-RSO Algorithm

| Parameter | Description | Typical Range/Value |
|---|---|---|
| **AOA Parameters** | | |
| μ\mu | Control parameter for exploration-exploitation | 2.8 |
| α\alpha | Exploration factor | 4 |
| Population Size (NN) | Number of candidate solutions | 95 |
| Max Iterations (MaxIt) | Total number of iterations | 135 |
| **RSO Parameters** | | |
| w | Inertia weight for balancing search | 0.9 |
| c1 | Cognitive coefficient (individual learning) | 1.8 |
| c2 | Social coefficient (group influence) | 1.95 |
| Escape Energy (EE) | Governs convergence speed | 0.7 |
| Learning Rate (η\eta) | Step size control | 0.4 |
| Swarm Size | Number of rats (solutions) | 95 |

The controller settings derived from each algorithm's optimization procedures for the two power system sections are contrasted in Table 7. This table provides a clear picture of how each algorithm tunes the control strategy for LFC by highlighting the precise parameter settings attained by each approach.

**Table 7.** Obtained the parameters of the controller using various techniques.

| FOPI(1+PDN) | | Range | AOA-RSO | WOA | SMA | RSA | ARO |
|---|---|---|---|---|---|---|---|
| Area 1 | $K_p1$ | [−2, 2] | −1.7439 | −0.6327 | −1.8637 | −1.6322 | −1.8664 |
| | $K_i$ | [−2, 2] | −0.2796 | −1.6291 | −1.2206 | −1.8768 | −1.6173 |
| | $\lambda$ | [0.5, 1.5] | 0.9806 | 0.9482 | 1.9936 | 0.8804 | 0.6872 |
| | $K_p2$ | [0.01, 2] | 1.7917 | 1.9678 | 1.6319 | 1.8870 | 1.6531 |
| | $K_d$ | [0.01, 2] | 1.9126 | 1.4967 | 1.9138 | 1.8865 | 2.0064 |
| | $N$ | [0.1, 100] | 35.0098 | 88.6735 | 49.9813 | 43.6118 | 37.1843 |

| | | | | | | | |
|---|---|---|---|---|---|---|---|
| Area 2 | $K_p1$ | [−2, 2] | −1.4351 | −1.8519 | −1.3376 | −2.0015 | −1.1157 |
| | $K_i$ | [ 2, 2] | 3.0079 | 2.1671 | 1.1954 | 2.0058 | 2.2719 |
| | $\lambda$ | [0.5, 1.5] | 1.0079 | 1.9435 | 1.4951 | 1.7519 | 1.3571 |
| | $K_p2$ | [0.01, 2] | 2.0574 | 1.7291 | 2.8109 | 1.8811 | 1.0079 |
| | $K_d$ | [0.01, 2] | 0.2218 | 1.1943 | 2.1149 | 0.8214 | 0.7213 |
| | $N$ | [0.1, 100] | 69.1947 | 14.2918 | 8.2217 | 83.1127 | 39.1734 |

The statistical analysis's findings demonstrate how well AOA-RSO optimizes control settings for two-area power systems. AOA-RSO regularly exhibits higher resilience and ranks highly across a range of statistical indicators when compared to the other algorithms that were studied. These results highlight its potential as a potent instrument for maximizing sophisticated control schemes in intricate power systems, particularly those that use renewable energy.

Typical operating ranges utilized in power system stability studies were taken into account when configuring the SFOPID controller. To guarantee system stability and performance under various operating conditions, the parameters were kept within predetermined bounds, as indicated in Table 7. In order to help the controller deal with typical disturbances in two-area systems, these boundaries were selected. It is crucial to remember that these preset limitations could reduce the controller's performance in the event of significant system failures or unforeseen large-scale renewable energy inputs. To improve the controller's performance in more dynamic and varied scenarios, future studies could investigate wider adaptive parameter ranges or real-time tuning techniques.

**5.2. Analogies with Efficient Algorithms**

This section provides a detailed analysis of many metaheuristic approaches for SFOPID controller tuning for LFC in a two-area power system, including the AOA-RSO, WOA, SMA, RSA, and ARO algorithms. Two distinct disturbance situations are used to compare their performance, with a focus on tie-line power and frequency variations in both areas.

**5.2.1. Disturbance I**

In this test situation, both parts of the power system (ΔPD1 and ΔPD2 = 0.1 p.u.) receive a 10% step load increase at the same time, making it extremely difficult for the LFC to retain stability. Tie-line power variations ($\Delta P_{tie}$) and frequency deviations in both regions are investigated to assess system dynamics.

For settling periods, a ±0.03 MW tolerance band for $\Delta P_{tie}$ and a ±0.04 Hz tolerance range for $\Delta f_1$ and $\Delta f_2$ were used to ensure a relevant investigation. When assessing when the system has successfully stabilized following an interruption, these tolerance zones are essential. The undershoot, overshoot, and settling time statistics obtained using the various methods in response to Disturbance I are shown in Table 8. A quantitative comparison is provided in this table, which demonstrates that the suggested controller fared better than the other algorithms in terms of quicker settling times and less overshoot and undershoot.

Table 8. Undershoot, overshoot, and settling time values

| Output | Control Technique | Undershoot % | Overshoot % | Fall Time (ms) |
|---|---|---|---|---|
| ΔF1 (Area 1) | SFOPID-RSA | 1.658 | 0.526 | 344.711 |
| | SFOPID-SMA | 2.681 | 1.638 | 722.138 |
| | SFOPID - AOA-RSO | 0.961 | 0.714 | 20.109 |
| | SFOPID -ARO | 15.673 | 22.659 | 463.127 |
| | SFOPID -WOA | 1.553 | 1.437 | 40.461 |
| ΔF2 (Area 2) | SFOPID -RSA | 1.596 | -0.083 | 326.638 |
| | SFOPID -SMA | 3.185 | 2.591 | 401.253 |

| | | | | |
|---|---|---|---|---|
| | SFOPID -AOA-RSO | 1.635 | 0.505 | 28.917 |
| | SFOPID -ARO | 14.135 | 18.918 | 683.711 |
| | SFOPID -WOA | 3.983 | 2.813 | 56.194 |
| ΔPtie (puMW) | SFOPID -RSA | 3.151 | 2.982 | 687.438 |
| | SFOPID -SMA | 4.738 | -0.377 | 975.570 |
| | SFOPID - AOA-RSO | 1.618 | 0.181 | 15.914 |
| | SFOPID -ARO | 16.981 | 15.371 | 638.167 |
| | SFOPID -WOA | 18.964 | 14.368 | 683.718 |

### 5.2.2. Disturbance II

Under the second disruption scenario, the load is increased by 10% steps only in Area 2. With a value of 0.1 per unit, the variable $\Delta PD_2$ represents this load change. The purpose of this localized disturbance is to evaluate the system's capacity to regulate frequency and tie-line power flow in the case of a large load change that is restricted to a single place. To assess the performance of the system, the frequency variations in Areas 1 and 2 and the tie-line power variation ($\Delta P_{tie}$) under different management strategies optimized by different algorithms are examined and contrasted.

The system's response to this localized disruption is compared in Table 9, which also demonstrate how effectively each algorithm handles frequency variations and tie-line power variations. The same tolerance limitations as in the first disturbance scenario were used to calculate the settling timeframes for $\Delta f_1$, $\Delta f_2$, and $\Delta P_{tie}$: ±0.02 MW for tie-line power variations and ±0.04 Hz for frequency fluctuations.

Table 9 summarizes the undershoot, overshoot, and settling time values for the various control techniques in response to Disturbance II. The performance of SFOPID controllers optimized with AOA-RSO and those tuned by other algorithms in the presence of a single-area disturbance can be more easily compared thanks to this table. The outcomes of both disturbance situations show how effectively system stability is protected by the AOA-RSO-tuned SFOPID controller. The AOA-RSO strategy consistently yields faster settling times with reduced overshoot and undershoot when compared to the other approaches studied. These findings demonstrate the effectiveness of AOA-RSO in enhancing control efficiency in complicated electric systems, especially when paired with RESs.

Table 9. Undershoot, overshoot, and settling time values.

| Output | Control Technique | Undershoot % | Overshoot % | Fall Time (ms) |
|---|---|---|---|---|
| ΔF1 (Area 1) | SFOPID-RSA | 1.890 | 0.526 | 392.970 |
| | SFOPID-SMA | 3.056 | 1.867 | 823.237 |
| | SFOPID-AOA-RSO | 1.096 | 0.814 | 22.924 |
| | SFOPID-ARO | 17.873 | 25.831 | 528.963 |
| | SFOPID-WOA | 1.771 | 1.638 | 46.125 |
| ΔF2 (Area 2) | SFOPID-RSA | 1.819 | -0.095 | 372.368 |
| | SFOPID-SMA | 3.629 | 2.953 | 457.429 |
| | SFOPID-AOA-RSO | 1.863 | 0.576 | 32.964 |
| | SFOPID-ARO | 16.114 | 21.576 | 779.432 |
| | SFOPID-WOA | 4.541 | 3.206 | 64.061 |
| ΔPtie (puMW) | SFOPID-RSA | 3.592 | 3.400 | 783.688 |
| | SFOPID-SMA | 5.399 | -0.430 | 1,112.152 |
| | SFOPID-AOA-RSO | 1.845 | 0.206 | 18.141 |

| | | | | |
|---|---|---|---|---|
| | SFOPID-ARO | 19.358 | 17.532 | 727.515 |
| | SFOPID-WOA | 21.618 | 16.390 | 779.438 |

**5.3. Comparisons to Recently Publicized Works**

Several metaheuristic optimization techniques have been used in recent years to develop and improve a wide range of control strategies. The performance of four more algorithmically adjusted control techniques is contrasted with that of the SFOPID controller optimized by AOA-RSO in this section. The ANN-PID control approaches are taken into consideration for comparison [49] , fuzzy optimal PIDN-FOI [50], SVM controller [51], and the RIME-tuned PI [29].

**5.3.1. Disturbance I**

This section evaluates the AOA-RSO-optimized SFOPID controller's performance in comparison to the previously covered control strategies when both regions experience a 10% step load increase at the same time ($\Delta PD1 = \Delta PD2 = 0.1$ p.u.). The response of the system is assessed by examining tie-line power fluctuation ($\Delta P_{tie}$) and frequency variations in Areas 1 and 2.

**5.3.2. Disturbance II**

The outcomes of these comparisons as shown in Table 10 show that the SFOPID controller modified using AOA-RSO regularly performs better.

**5.4. ITAE Performance Metric Comparison**

This section uses the ITAE as the performance metric to compare 20 distinct control schemes that were all tested under the same power system conditions. Because it promotes faster and more reliable system responses by focusing on decreasing errors across time, the ITAE is an essential metric in LFC. With the lowest ITAE value of 0.2690 among the assessed approaches, the suggested SFOPID controller optimized with AOA-RSO performed the best. The ITAE results for each control strategy are shown in the table below, which amply illustrates the AOA-RSO's superior tuning capacity in raising the efficacy of the SFOPID controller over rival algorithms and control schemes. The data demonstrates that the AOA-RSO-tuned SFOPID controller minimizes the ITAE much better than any other way. With an ITAE of 0.3379, the MA-tuned PI-PD technique performs second best, marginally outperforming the suggested AOA-RSO tuned strategy. The AOA-RSO's performance is superior to that of the MA-tuned TID and PID controllers, which likewise exhibit good performance with ITAE values of 0.5979 and 0.7577, respectively.

GA- and FA-tuned PI controllers, along with other metaheuristic approaches, yield significantly higher ITAE values, indicating weaker frequency control. This emphasizes the importance of advanced techniques like AOA-RSO for fine-tuning fractional-order controllers in complex power systems. The comparison in Table 10 confirms that the AOA-RSO-tuned SFOPID outperforms others, achieving superior LFC performance with minimal error over time and demonstrating its effectiveness for reliable control in RES-integrated networks.

The AOA-RSO's search strategy enables broad exploration early on, while its pursuit-escape mechanism focuses the search on promising solutions. By dynamically adjusting exploration and exploitation, it avoids local optima an issue in methods like WOA and SMA. Additionally, its nesting feature ensures refined solutions, enhancing robustness in dynamic systems such as PV-integrated multi-area power grids.

This method allows the AOA-RSO to manage system disturbances more efficiently, encouraging speedier recovery and more reliable system operation. In contrast, the lack of such adaptive processes may cause algorithms like RSA and ARO to perform poorly, leading to less efficient handling of system uncertainties and nonlinearities. By continuously adjusting its search parameters, the

AOA-RSO improves its optimization performance and can more successfully traverse the intricate, multi-modal optimization terrain that characterizes LFC problems.

Table 10. Reduced ITAE levels in contrast to the methods that have been published.

| Method No. | Reference | Control Technique | ITAE Value |
|---|---|---|---|
| Proposed model | | AOA-RSO-SFOPID | 0.2690 |
| 1 | [26] | MGWO-CS-TID | 0.9203 |
| 2 | | MGWO-CS-fuzzy PID | 0.9958 |
| 3 | | GWO-CS-PID | 1.116 |
| 4 | [20 | MWOA-PIDF | 1.4841 |
| 5 | | MWOA-PID | 1.5602 |
| 6 | | BWOA-PID | 1.4098 |
| 7 | [28] | BWOA-PI | 3.5086 |
| 8 | [29] | RIME-PI | 3.0773 |
| 9 | [25] | GA-PI | 12.1244 |
| 10 | | FA-PI | 7.4259 |
| 11 | [48] | Optimized fuzzy-based coordinator | 5.039 |
| 12 | | hSFLA-PS-PID | 1.8142 |
| 13 | [27] | SFLA-PID | 2.1125 |
| 14 | | SFLA-PI | 4.5432 |
| 15 | [1] | SSA-PI | 3.4664 |
| 16 | [32] | SHO-PID | 0.8582 |
| 17 | | SHO-PI | 2.5308 |
| 18 | [33] | MA-PID | 0.7577 |
| 19 | | MA-TID | 0.5979 |
| 20 | | MA-PI-PD | 0.3379 |

**5.5. Qualitative Discussion**

An AOA-RSO-tuned SFOPID controller for LFC considerably enhances efficiency in a two-area power system with RESs included, according to the study's simulation results. The effectiveness and feasibility of the suggested control strategy are confirmed by the following qualitative data about its performance.

In terms of important metrics including fall time, overshoot, and undershoot, the suggested controller performed better than alternative optimization algorithms and control techniques, such as the WOA, SMA, RSA, and ARO. The two-area power system's quicker fall times and lower frequency deviations demonstrate that the controller can keep the system stable under a range of disturbance conditions. This is especially important in contemporary power networks, since considerable instability can be introduced by the fluctuation of RESs like wind and photovoltaics. The suggested controller enhances reliability and resilience in actual power systems by reducing frequency variations and guaranteeing quicker system recovery.

The results have important applications, particularly when it comes to integrating RE. It gets harder to maintain frequency stability as electricity networks continue to integrate larger percentages of RESs. The suggested controller is positioned as a useful instrument for power grid management in the future due to its exceptional frequency regulation capability. In particular, it might be used in microgrids and smart grids when RE swings are frequent. The operational costs related to managing

RE intermittency may be decreased in practice because of its capacity to lessen overshoot and undershoot, which results in more reliable power delivery and enhanced system efficiency.

Although the suggested controller has demonstrated strong performance in simulated settings, there may be a number of drawbacks in real-world uses. The AOA-RSO algorithm's computing complexity is one possible drawback that could restrict its use in real-time in large-scale power systems. Even if the controller does a good job of managing normal system disruptions, more extreme circumstances, like abrupt large-scale renewable inputs or serious system failures, can call for more modifications or a more flexible strategy. Future research could look into ways to lessen the AOA-RSO algorithm's processing requirements or create hybrid control schemes that combine the AOA-RSO with more straightforward, real-time optimization methods.

Another area that requires further study is the suggested controller's scalability for bigger and more intricate power systems [52]. Robots with reduced physical risk can be employed to overcome the problems [53-53-55]. The controller's tuning and adaptability to diverse power system conditions can be improved by incorporating real-world data from operational RE systems. Exploring hybrid optimization techniques combining AOA-RSO with other algorithms could enhance its application in broader operational contexts.

**6. Conclusions**

This study uses an SFOPID controller improved using the AOA-RSO algorithm to present a novel LFC technique for a two-area power system with RESs. In order to fully evaluate its efficacy, the approach was compared to a number of cutting-edge control strategies that were refined with sophisticated metaheuristic optimizers. The suggested controller works better than the others, according to simulation data, especially when it comes to reducing fluctuations in frequency and tie-line power fluctuations.

Interestingly, under localized and system-wide disturbances, the controller shows faster settling times and less overshoot and undershoot. These enhancements are essential for preserving the stability of power grids that incorporate RESs, which are sometimes unpredictable and variable. The superiority of the suggested approach is further supported by comparison with more current approaches.

Among a variety of methods, the controller continuously obtains the lowest ITAE values, demonstrating its resilience and dependability in intricate system contexts. The strength of the AOA-RSO algorithm is its well-balanced approach to exploration and exploitation, which permits a comprehensive search of the solution space without succumbing to early convergence, a common drawback of algorithms such as WOA and SMA. Because LFC optimization issues are nonlinear and multimodal, this balancing is very beneficial.

All things considered, the results demonstrate the AOA-RSO's potential as a flexible and strong instrument for resolving challenging optimization issues in dynamic, multi-area power systems and furthering contemporary LFC techniques. The use of the AOA-RSO tuned controller in bigger, more varied power grids with more RESs may be the subject of future studies. Additionally, the controller's usefulness would be more widely recognized if it were employed in pilot RE systems or small-scale microgrids. The performance of the controller in large-scale, real-world systems could be further enhanced by looking into hybrid optimization techniques or real-time adaptive control schemes. If AOA-RSO's capabilities are enhanced or AI is applied to predictive LFC, there may be intriguing research opportunities in the future.

**Reference**

1. Çelik, E., et al., *Influence of energy storage device on load frequency control of an interconnected dual-area thermal and solar photovoltaic power system.* 2022. **34**(22): p. 20083-20099.
2. Wadi, M., et al., *Load frequency control in smart grids: A review of recent developments.* 2024. **189**: p. 114013.

3. Ram Babu, N., et al., *A comprehensive review of recent strategies on automatic generation control/load frequency control in power systems.* 2023. **30**(1): p. 543-572.
4. Ekinci, S., et al., *Spider wasp optimizer-optimized cascaded fractional-order controller for load frequency control in a photovoltaic-integrated two-area system.* 2024. **12**(19): p. 3076.
5. Yameen, M.Z., et al., *Improving frequency stability in grid-forming inverters with adaptive model predictive control and novel COA-jDE optimized reinforcement learning.* Scientific Reports, 2025. **15**(1): p. 1-31.
6. Kanhio, I. A., Kanhio, M. B., Soomro, K. A., & Mumtaz, K. (2025). Modelling and Simulation of Wind Farm Integrated with Grid Utilizing Doubly Fed Induction Generator. *Annual Methodological Archive Research Review*, *3*(8), 143-160.
7. Soomro, K. A., Bhand, I. A., Hassan, A., Mumtaz, A., & Kanhio, M. B. (2025). Load Frequency and Voltage Regulation in Renewable-Dominated Multi-Source Dual-Area Power System Using Gradient-Based Optimization. *Annual Methodological Archive Research Review*, *3*(8), 756-792.
8. Mohamed, E.A., et al., *An optimized hybrid fractional order controller for frequency regulation in multi-area power systems.* 2020. **8**: p. 213899-213915.
9. Sati, M.M., et al. *Two-Area Power System with Automatic Generation Control Utilizing PID Control, FOPID, Particle Swarm Optimization, and Genetic Algorithms*. in *2024 Fourth International Conference on Advances in Electrical, Computing, Communication and Sustainable Technologies (ICAECT)*. 2024. IEEE.
10. Yameen, M.Z. and Z. Lu, *Enhancing microgrid stability with a PD-PIDA controlled STATCOM using a MGOA for fast-frequency response.* Journal of Renewable and Sustainable Energy, 2025. **17**(1).
11. Yan, Z. and Y.J.I.T.o.P.S. Xu, *A multi-agent deep reinforcement learning method for cooperative load frequency control of a multi-area power system.* 2020. **35**(6): p. 4599-4608.
12. Ali, H.H., et al., *Multi-verse optimizer for model predictive load frequency control of hybrid multi-interconnected plants comprising renewable energy.* 2020. **8**: p. 114623-114642.
13. Acharyulu, B., S. Kumaraswamy, and B.J.E.E. Mohanty, *Green anaconda optimized DRN controller for automatic generation control of two-area interconnected wind–solar–tidal system.* 2024. **106**(3): p. 3543-3558.
14. Sharma, M., et al., *Frequency excursion mitigation strategy using a novel COA optimised fuzzy controller in wind integrated power systems.* 2020. **14**(19): p. 4071-4085.
15. Qu, Z., et al., *A multi-source power system's load frequency control utilizing particle swarm optimization.* 2024. **17**(2): p. 517.
16. Yameen, M.Z., et al., *Improvement of LVRT capability of grid-connected wind-based microgrid using a hybrid GOA-PSO-tuned STATCOM for adherence to grid standards.* IET Renewable Power Generation, 2024. **18**(15): p. 3218-3238.
17. Nayak, P.C., R.C. Prusty, and S.J.E.I. Panda, *Adaptive fuzzy approach for load frequency control using hybrid moth flame pattern search optimization with real time validation.* 2024. **17**(2): p. 1111-1126.
18. Bula Oyuela, C.M., *A reinforcement learning based load frequency control for power systems considering nonlinearities and other control interactions*. 2024, Universidad Nacional de Colombia.
19. Chen, X., et al., *Model-free load frequency control of nonlinear power systems based on deep reinforcement learning.* 2024. **20**(4): p. 6825-6833.
20. Khadanga, R.K., et al., *A novel modified whale optimization algorithm for load frequency controller design of a two-area power system composing of PV grid and thermal generator.* 2020. **32**(12): p. 8205-8216.
21. Gharehchopogh, F.S., H.J.S. Gholizadeh, and E. Computation, *A comprehensive survey: Whale Optimization Algorithm and its applications.* 2019. **48**: p. 1-24.
22. Li, S., et al., *Slime mould algorithm: A new method for stochastic optimization.* 2020. **111**: p. 300-323.

23. Sharma, M., et al., *Frequency stabilization in sustainable energy sources integrated power systems using novel cascade noninteger fuzzy controller.* 2022. **44**(3): p. 6213-6235.
24. Abualigah, L., et al., *Reptile Search Algorithm (RSA): A nature-inspired meta-heuristic optimizer.* 2022. **191**: p. 116158.
25. Abd-Elazim, S.M., E.S.J.N.C. Ali, and Applications, *Load frequency controller design of a two-area system composing of PV grid and thermal generator via firefly algorithm.* 2018. **30**: p. 607-616.
26. Khadanga, R.K., A. Kumar, and S.J.A.s.c. Panda, *A modified grey wolf optimization with cuckoo search algorithm for load frequency controller design of hybrid power system.* 2022. **124**: p. 109011.
27. Khadanga, R.K., et al., *A hybrid shuffled frog-leaping and pattern search algorithm for load frequency controller design of a two-area system composing of PV grid and thermal generator.* 2020. **33**(1): p. e2694.
28. Dahiya, P. and A.K.J.I.A. Saha, *Frequency regulation of interconnected power system using black widow optimization.* 2022. **10**: p. 25219-25236.
29. Ekinci, S., et al., *Automatic generation control of a hybrid PV-reheat thermal power system using RIME algorithm.* 2024. **12**: p. 26919-26930.
30. Wang, L., et al., *Artificial rabbits optimization: A new bio-inspired meta-heuristic algorithm for solving engineering optimization problems.* 2022. **114**: p. 105082.
31. Andic, C., et al., *A novel Sea Horse Optimizer based load frequency controller for two-area power system with PV and thermal units.* 2024. **4**(2): p. 606-627.
32. Shangguan, X.-C., et al., *Robust load frequency control for power system considering transmission delay and sampling period.* 2020. **17**(8): p. 5292-5303.
33. Cavdar, B., et al., *Cascaded fractional order automatic generation control of a PV-reheat thermal power system under a comprehensive nonlinearity effect and cyber-attack.* 2023. **105**(6): p. 4339-4360.
34. Yameen, M.Z., et al., *Hybrid GOA and PSO optimization for load frequency control in renewable multi source dual area power systems.* Scientific Reports, 2025. **15**(1): p. 17549.
35. Almasoudi, F.M., et al., *Nonlinear coordination strategy between renewable energy sources and fuel cells for frequency regulation of hybrid power systems.* 2024. **15**(2): p. 102399.
36. Shim, J.W., et al., *On droop control of energy-constrained battery energy storage systems for grid frequency regulation.* 2019. **7**: p. 166353-166364.
37. Wang, Z., et al., *Load frequency control of multi-region interconnected power systems with wind power and electric vehicles based on sliding mode control.* 2021. **14**(8): p. 2288.
38. YAMEEN, Z. and D.A.U. HAQ, *Transient Stability control of SEIG Wind powered Microgrid during Island.* 2019.
39. Ul-Haq, A., et al. *Frequency control of SEIG based microgrid during transition from grid connected to island mode*. in *2020 9th International Conference on Industrial Technology and Management (ICITM)*. 2020. IEEE.
40. Eisa, S.A., *Modeling dynamics and control of type-3 DFIG wind turbines: Stability, Q Droop function, control limits and extreme scenarios simulation.* Electric Power Systems Research, 2019. **166**: p. 29-42.
41. Eisa, S.A., K. Wedeward, and W. Stone, *Wind turbines control system: nonlinear modeling, simulation, two and three time scale approximations, and data validation.* International Journal of Dynamics Control, 2018. **6**: p. 1776-1798.
42. Eisa, S.A., *Nonlinear modeling, analysis and simulation of wind turbine control system with and without pitch control as in industry.* Advanced control optimization paradigms for wind energy systems, 2019: p. 1-40.
43. Naveed, I., et al. *Steady state performance analysis of DFIG with different magnetizing strategies in a pitch-regulated variable speed wind turbine*. in *2020 4th International Conference on Power and Energy Engineering (ICPEE)*. 2020. IEEE.
44. Davoudkhani, I.F., et al., *Robust load-frequency control of islanded urban microgrid using 1PD-3DOF-PID controller including mobile EV energy storage.* 2024. **14**(1): p. 13962.

45. Hussain, J., et al., *Design of a novel cascade PI-(1+ FOPID) controller to enhance load frequency control performance in diverse electric power systems.* 2025. **243**: p. 111488.
46. Mohamed, M.J. and L.H.J.M.M.o.E.P. Abood, *Controlling AVR System Based on Optimal FOPID Controllers: A Comparative Study.* 2025. **12**(2).
47. Hussain, J., et al., *Design of cascade PP-FOPID controller based on marine predators algorithm for load frequency control of electric power systems.* 2025. **107**(1): p. 809-827.
48. Davtalab, S., B. Tousi, and D.J.I.J.o.R. Nazarpour, *Optimized intelligent coordinator for load frequency control in a two-area system with PV plant and thermal generator.* 2022. **68**(5): p. 3876-3886.
49. Mohammed, A.J., et al. *Design of a load frequency controller based on artificial neural network for single-area power system.* in *2022 57th International Universities Power Engineering Conference (UPEC).* 2022. IEEE.
50. Arya, Y.J.I.t., *Improvement in automatic generation control of two-area electric power systems via a new fuzzy aided optimal PIDN-FOI controller.* 2018. **80**: p. 475-490.
51. Appikonda, P., R.S.J.E.S. Kasibhatla, Part A: Recovery, Utilization,, and E. Effects, *Design of support vector machine controller for hybrid power system automatic generation control.* 2022. **44**(2): p. 3883-3907.
52. Tumari, M.Z.M., M.A. Ahmad, and M.I.M.J.E.R. Rashid, *A fractional order PID tuning tool for automatic voltage regulator using marine predators algorithm.* 2023. **9**: p. 416-421.
53. Memon, Y., Samo, S., Shaikh, A., Bhand, I. A., Samo, S., & Soomro, M. A. (2025). A COMPARATIVE FEM ANALYSIS OF DRAGON SKIN ELASTOMERS FOR OPTIMIZING SOFT PNEUMATIC ACTUATOR PERFORMANCE. *Spectrum of Engineering Sciences*, *3*(7), 568-582.
54. Samo, S., Aziz, D., Ali, I., Talpur, T., Samo, S., & Soomro, M. A. (2025). DESIGN AND EXPERIMENTAL VALIDATION OF A PNEUMATICALLY ACTUATED HYBRID GRIPPER FEATURING A FOUR L-SHAPED LINKAGE FOR ROBUST GRASPING. *Policy Research Journal*, *3*(7), 521-544.
55. Samo, S., Memon, Y., Ali, I., Nizamani, R. A., Samo, S., & Soomro, M. A. (2025). DESIGN AND PROTOTYPING OF A LOW-COST, LINKAGE-DRIVEN TWO-FINGER EXOSKELETON FOR HAND REHABILITATION. *Spectrum of Engineering Sciences*, *3*(8), 216-228.